



Inorganic–organic core–shell titania nanoparticles for efficient visible light activated photocatalysis

N.G. Moustakas^a, A.G. Kontos^a, V. Likodimos^a, F. Katsaros^a, N. Boukos^a, D. Tsoutsou^a, A. Dimoulas^a, G.E. Romanos^a, D.D. Dionysiou^b, P. Falaras^{a,*}

^a Institute of Advanced Materials, Physicochemical Processes, Nanotechnology and Microsystems (IAMPNNM), Division of Physical Chemistry,

National Center for Scientific Research "Demokritos", 153 10 Aghia Paraskevi Attikis, Athens, Greece

^b Environmental Engineering and Science Program, University of Cincinnati, Cincinnati, OH 45221, USA

ARTICLE INFO

Article history:

Received 1 August 2012

Received in revised form 5 October 2012

Accepted 11 October 2012

Available online 23 October 2012

Keywords:

Visible light active TiO₂

Core–shell structure

Solar photocatalysis

HRTEM

EPR

ABSTRACT

Nanostructured modified TiO₂ (m-TiO₂) was synthesized using the gel combustion method based on the calcination of an acidified alkoxide solution mixed with urea. The materials were characterized by Raman, FT-IR and UV-vis diffuse reflectance spectroscopies, transmission (TEM) and scanning electron microscopies (SEM), X-ray photoelectron spectroscopy (XPS) and electron paramagnetic resonance (EPR), in comparison with reference material untreated with urea (ref-TiO₂). The effect of both the urea content and calcination temperature were optimized, providing the optimal absorption threshold of 2.19 eV for solar light harvesting. The photocatalytic performance of the m-TiO₂ powder was tested for the degradation of methylene blue (MB) azo dye under UVA (350–365 nm), visible (440–460 nm), and daylight (350–750 nm) illumination. The hybrid inorganic/organic material shows exceptional physicochemical properties and significant photocatalytic activity, especially in the visible, attributed to sensitization of the TiO₂ by a thin porous layer of carbonaceous species in controlled core–shell morphology.

© 2012 Elsevier B.V. All rights reserved.

1. Introduction

Since the pioneering discovery on the photo-electrochemical water splitting using titanium dioxide (TiO₂) by Fujishima and Honda [1], TiO₂ photocatalysis has emerged as a promising clean advanced oxidation technology (AOT), which could address the ever increasing global concerns for environmental pollution abatement based on the utilization of solar energy [2]. Ample verification of the effectiveness of TiO₂ to generate highly reactive chemical species (e.g., hydroxyl radicals) upon UV light illumination along with its environmentally benign properties and relatively low cost, rendered TiO₂ a key material for the non-selective destruction of organic pollutants in water and air. However, despite the marked progress in the development of TiO₂ photocatalytic materials, their practical application is challenged by two inherent properties of titania, namely the low quantum yield and mainly the wide band gap of TiO₂ that limits its response to the UVA spectral range (<400 nm). During the last decade, extension of the TiO₂ photoreponse into the visible region and exploitation of solar light driven applications have become a topic of great interest. To this end,

various approaches [3] were used including bulk or surface anion doping of TiO₂ [4–6], defect activation, the 'black TiO₂' approach that relies on a crystalline core/disordered shell morphology [7] and co-sensitization of TiO₂ with inorganic or organic compounds [8,9].

Nitrogen doping via sol gel synthesis using diverse anion precursors (amines, nitrates, ammonium salts, ammonia and urea) [4], has been verified as a very efficient modification route of TiO₂ photocatalyst, activated in the visible via the formation of localized energy states within titania's band gap or even oxygen vacancies created during the reaction with the anion precursor [10]. Three possible scenarios, including substitutional or interstitial N doping and defects formed due to disorder in the nanoparticle surface are sketched in Fig. 1a–c. An alternative route for the visible light activation of TiO₂ has been recently put forward based on the calcination of titania in the presence of urea [11]. The resulting materials were shown to consist of a titania core covered by a poly(tri-s-triazine) shell, in situ formed on the TiO₂ surface by the thermal decomposition of urea [12], as sketched in Fig. 1d. The urea-derived TiO₂ was highly active in the degradation of formic acid under visible light due to the polymeric carbon-nitride acting as a photosensitizer that simultaneously promoted the stabilization of photo-generated holes, circumventing the weak oxidation ability of N-doped TiO₂ produced by other methods. A modified approach was originally followed by our group [13], relying on the insertion

* Corresponding author. Tel.: +30 2106503644; fax: +30 2106511766.

E-mail address: papi@chem.demokritos.gr (P. Falaras).

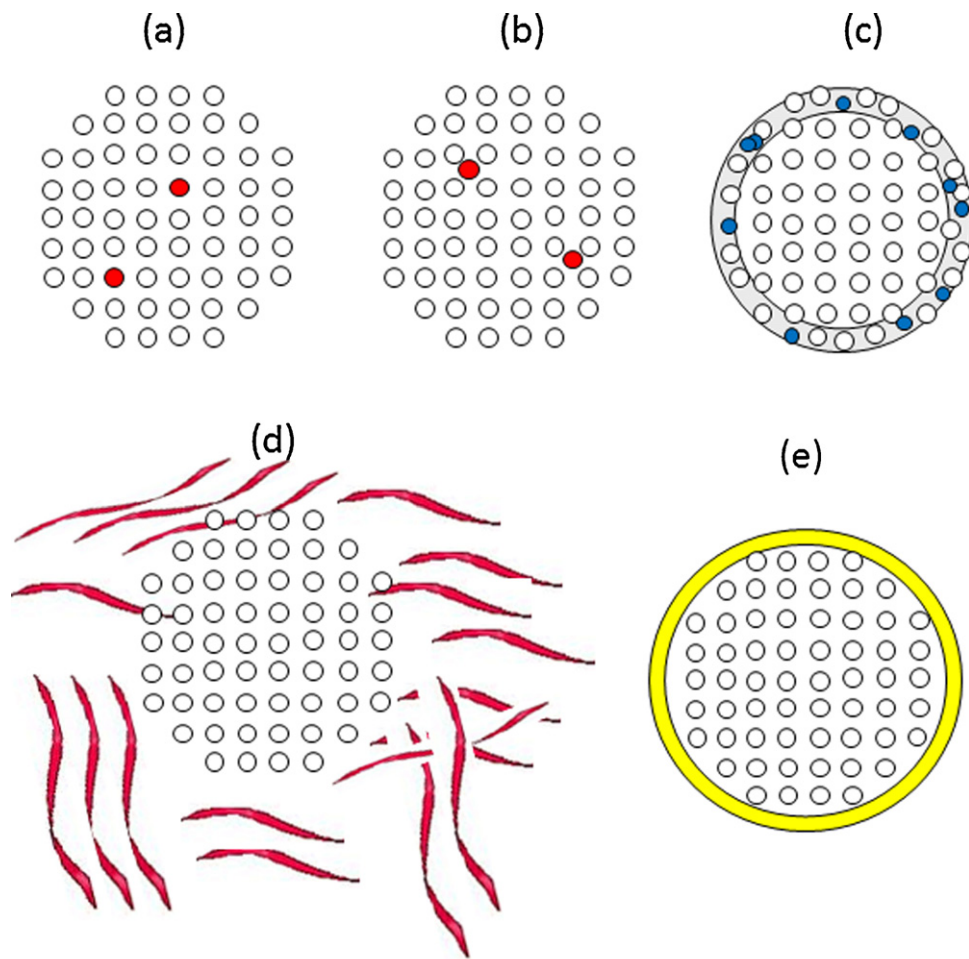


Fig. 1. Sketch of possible modification routes for TiO₂ to become visible light active: (a) substitutional N doping, (b) interstitial N doping, (c) defect formation by surface doping, (d) polymeric carbon-nitride/TiO₂ composite structure and (e) sensitization of the surface by carbonaceous species in the form of a surface capping layer.

of urea in nitrated titania followed by calcination at 350–450 °C. In this approach, urea is neither the precursor for the N doping nor the source of a graphitic carbon nitride forming a composite with TiO₂ but on the contrary it is inserted during the gelation process and controls drastically the materials growth and properties (nanoparticles size, porosity and surface modification). This particular methodology has been identified as a sol-gel combustion synthesis of TiO₂ [14] and has been applied in the synthesis of visible-light-active (VLA) semiconductor photocatalysts, including TiO₂ [15,16] and ZnO [17]. Among the advantages of the method are its simplicity and reliability, growth of highly porous materials due to the evolution of large amounts of gases during the reaction and avoidance of calcination at high temperature. The process is based on three steps: (a) the hydrolysis of the alkoxide, (b) the nitration reaction to form Ti(NO₃)₂ and (c) the combustion reaction of the titanyl nitrate (oxidizer) with a suitable fuel (glycine, oxalic acid, urea and others) to formulate TiO₂ nanoparticles with N₂, CO₂ and H₂O as the reaction byproducts.

In the case of TiO₂ synthesis using the combustion method, although glycine is most frequently used as a fuel, a few reports with urea [18,19] have recently appeared in addition to our previous report [13]. In [18], sol-gel combustion was applied by varying the fuel (urea) to oxidizer (titanyl nitrate) ratio (φ); φ was found to determine the maximum combustion temperature, which in turn affects the specific surface area, crystallite size and fraction of the anatase phase in the synthesized titania particles. In [19], high 10:1 urea-titanyl nitrate molar concentration ratio was

used to prepare optimal materials in terms of high specific surface area (234 m²/g), small nanoparticle size (6.8 nm), wormhole mesoporosity and sunlight activated photocatalytic degradation of rhodamine-B. Although these works are systematic, the light absorption of the materials is limited to a tail in the visible spectral range, while their photocatalytic activity is only proven under solar light irradiation, precluding discrimination of the VLA activity and its firm correlation with the improved morphological and structural materials properties.

Generally, combustion synthesis results in the carbon modification of the TiO₂ surface, although both carbon [16] and nitrogen [19] doping have been also proposed. Surface modification of TiO₂ by carbonaceous species like carbon nanotubes, fullerenes, graphene oxide, and other nanocarbons mainly of graphitic type have led to significant enhancement of their photocatalytic activity [9,20]. This enhancement is essentially attributed to several factors: (a) sensitization of the material by a visible light absorber, (b) retardation of electron hole recombination via charge separation across the TiO₂-carbonaceous type sensitizer heterojunction, (c) significant increase of the surface area and the population of active photocatalytic sites and (d) increased amount of surface adsorbed molecules of chemical pollutants via $\pi-\pi$ interactions. The most advantageous morphology is the formation of a core/shell structure as that sketched in Fig. 1e where the sensitizer covers the TiO₂ nanoparticle with a thin homogenous wrapping layer, maximizing, in this way, heterojunction functionality without loss of light harvesting. Such an ideal structure was obtained in [21] by synthesizing

graphene crystalline-TiO₂ hybrids that show very high photocatalytic activity under visible light. Furthermore, it should be noted that aromatic carbon compounds have been also identified as the origin of visible light activity of commercial Kronos photocatalysts [22] where titania modification is carried out with pentaerythritol.

In this work, modified titania (m-TiO₂) was optimized using a volumetric type of smoldering combustion sol-gel synthesis employing urea as fuel and a post treatment purification of the photocatalyst. Both urea content and calcination temperature were optimized, providing the optimal absorption threshold of 2.19 eV for solar light harvesting. The photocatalytic performance of the m-TiO₂ powder was tested for the degradation of methylene blue under UVA (350–365 nm), visible (440–460 nm), and daylight (350–750 nm) illumination, showing significant photocatalytic activity. Thorough characterization of the materials with advanced spectroscopic and microscopic techniques attributes this activity to the formation of core crystalline TiO₂ nanoparticles covered uniformly with a shell of carbonaceous type material, which acts as a highly efficient visible light sensitizer. The photocatalytic reactivity further benefits by the enhanced adsorption of pollutant molecules via the high surface area, porosity and the chemical modification of the photocatalyst surface as well as by the retardation of recombination effects due to the small nanoparticle size and the improved charge separation at the inorganic/organic heterojunction.

2. Materials and methods

For the preparation of the modified TiO₂ photocatalysts, tetrabutylorthotitanate (15 ml) (Aldrich 97%) was added dropwise into 100 mL of HNO₃ acidified aquatic solution. After 4 h of vigorous stirring, n-propanol was added and the translucent colloidal solution became completely transparent. The solution was left overnight under vigorous stirring to homogenize. Then various amounts of urea (1–50 g), were added, with corresponding fuel to oxidizer ratios $0.38 < \varphi < 19$, followed by a first drying step at 100 °C and further calcination at the temperature range of 350–500 °C. The volumetric type flameless gel combustion resulted in the synthesis of nanoparticulate titania with vivid yellowish color. Finally, the photocatalyst underwent consecutive washings under vigorous stirring with deionized water in combination with centrifugation for removing the excess organic species. A reference sample (ref-TiO₂) was made following the same procedure without the use of urea. Elemental analysis of the samples resulted in C atomic concentration of 1–3% and N below 1%.

The crystallinity of the prewashed photocatalysts was analyzed with an X-ray diffractometer (Siemens D-500, Cu K α radiation). m-TiO₂ shows a single anatase phase while ref-TiO₂, in addition to the principal anatase phase, contains rutile as a second phase and traces of brookite, in full agreement with Raman scattering characterization. Thermogravimetric analysis and differential scanning calorimetry was performed on a SETARAM SETSYS Evolution 18 Analyser, in the range of RT – 800 °C, with a heating rate 5 °C/min in an alumina crucible using air. The recorded TGA and DSC curve on the m-TiO₂ (Fig. S1), showed significant weight loss at temperatures up to 450 °C. From the organic species that remain in the material at relatively low temperatures (350–450 °C) some are chemically bound to the TiO₂ surface, while others are expected to be removed in the persistent post washing treatment of the material. Nitrogen adsorption isotherms were measured at 77 K in an automated volumetric system (AUTOSORB-1-Krypton version – Quantachrome Instruments). Prior to their measurement, the samples were outgassed at 200 °C for 48 h. The Brunauer–Emmett–Teller (BET) specific surface area (S_{BET}) and Barrett–Joyner–Halenda (BJH) pore size distributions were

determined by the N₂ isotherms. UV-visible diffuse reflectance measurements were carried out employing a Hitachi 3010 spectrophotometer equipped with a 60-mm diameter integrating sphere and Ba₂SO₄ reference windows. The reflectance data were transformed in Kubelka–Munk absorbance units.

IR spectra were collected on a Thermo Scientific Nicolet 6700 FTIR with N₂ purging system. Spectra were acquired using a single reflection ATR (attenuated total reflection) SmartOrbit accessory equipped with a single-bounce diamond crystal (spectral range: 10,000–55 cm⁻¹, angle of incidence: 45°). A total of 32 scans were averaged for each sample and the resolution was 4 cm⁻¹. The spectra were obtained against a single-beam spectrum of the clean ATR crystal and converted into absorbance units. Data were collected in the range 4000–400 cm⁻¹. Raman spectroscopy was performed in backscattering configuration employing an Ar⁺ ion laser ($\lambda = 514.5$ nm) as excitation source by adjusting the laser power to 0.1 mW μm⁻² on a Renishaw InVia Reflex spectrometer.

Batches of unmodified and modified TiO₂ samples were examined utilizing a FEI CM20 TEM equipped with a Gatan GIF200 imaging filter for electron energy loss spectroscopy (EELS) and energy filtering analysis (EFTEM). The samples were dispersed on holey carbon TEM grids and the study was undertaken on agglomerates of particles on the holes of the grid in order to exclude the influence of the amorphous C support on the results. A Jeol JSM 7401F Field Emission Scanning Electron Microscope equipped with Gentle Beam mode and the new r-filter was employed to characterize the surface morphology of the developed materials. Gentle Beam technology can reduce charging and improve resolution, signal-to-noise, and beam brightness, especially at low beam voltages (down to 100 V), without gold plating.

Core-level X-ray photoemission (XPS) spectra were collected with a PHOIBOS 100 (SPECS) hemispherical analyzer at a pass energy of 15 eV with an Al X-ray source (1486.6 eV). The take-off angle was set at 37° relative to the sample surface. The binding energy scale was calibrated using the position of both the Au 4f_{7/2} and Ag 3d_{5/2} peaks at 84 and 368.3 eV, respectively measured on clean gold and silver foils. Electron paramagnetic resonance (EPR) measurements were performed using an X-band ($\nu \approx 9.42$ GHz) Bruker ER-200D spectrometer equipped with an Oxford ESR 900 cryostat for low temperature measurements. A LED source emitting at 440–460 nm was used for in situ visible light illumination of the sample in the EPR cavity.

In typical photocatalytic experiments, 20 ml of oxygenated aqueous methylene blue (MB) solution (2 mg/L) containing the photocatalyst (1 mg/ml) were added into a cylindrical pyrex cell and covered air tightly. The pyrex cell was placed in the center axis of a rectangular parallelepiped black box photoreactor (50 cm × 40 cm × 30 cm in dimensions) at a distance of 12 cm from the illumination system. The photocatalytic performance of the modified TiO₂ (as well as ref-TiO₂ and Evonik P25 used as reference materials) were examined using different light sources in a parallel symmetric arrangement on the top of the reactor: 9 high power Luxeon light emitting diodes (LEDs) emitting at the narrow royal blue spectral region (440–460 nm, 4.5 mW/cm²), 4 Sylvania GTE F15W/T8 lamps (350–390 nm, 0.5 mW/cm²) and 4 Sylvania 15 W daylight lamps (350–750 nm, 3 mW/cm²). In Fig. S2, the emission spectrum of the LED light source is compared with the absorbance spectrum of the optimum m-TiO₂ sample and that of the MB pollutant. Apparently, the LED light source emits well in the visible wavelength range (440–460 nm) where the m-TiO₂ material has intense light absorbance, whereas the MB pollutant hardly absorbs. Throughout the experiments (photocatalytic or control), the solutions were stirred to secure homogenous dispersion of the photocatalyst and minimize volume decreasing effects. Each experimental point corresponds to a new photocatalytic run that ended up with the sample drawn from the reaction vessel,

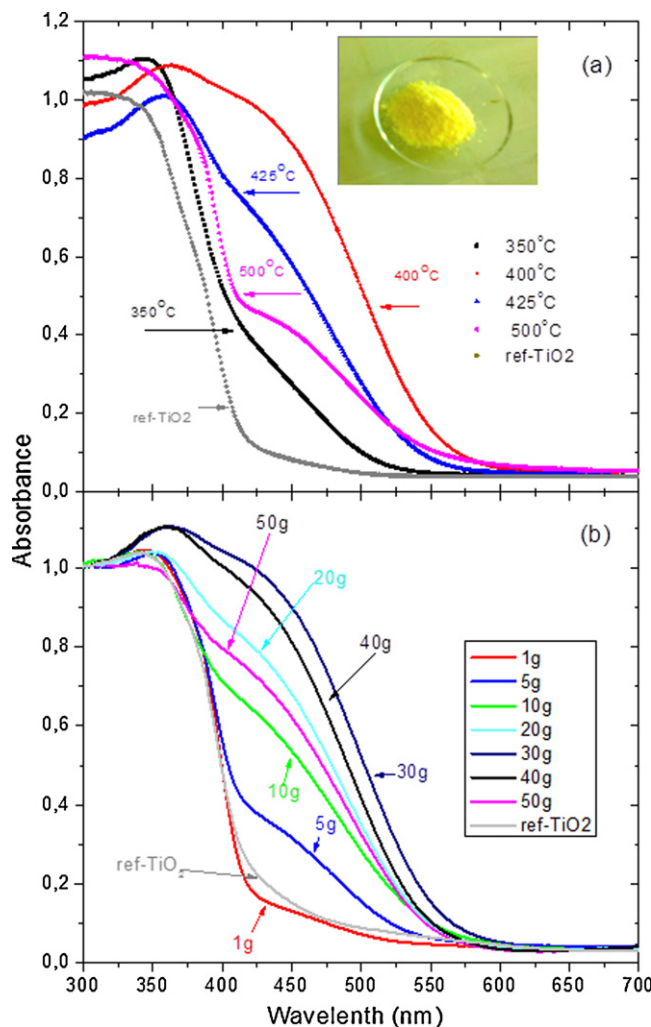


Fig. 2. UV-vis absorption spectra of the modified TiO₂ as a function (a) of the calcination temperature with 30 g of urea and (b) of the urea content at 400 °C. Photograph of the optimized modified TiO₂ powder is shown as an inset.

centrifuged at 9000 rpm for 40 min using a Universal 320 centrifuge to remove catalyst particles and monitoring the evolution of the MB concentration photometrically using a Hitachi U-3010 UV-vis spectrophotometer. Blank photocatalytic tests verified negligible reduction of the MB pollutant concentration upon irradiation with either visible or UV light in the absence of the photocatalyst.

3. Results and discussion

3.1. Optical response of the modified TiO₂

The UV-vis spectra of the ref-TiO₂ materials showed only a weak absorption tail in the visible spectral range, while those of the modified TiO₂ exhibited a distinct red shift of the optical absorption that depended markedly on the urea content and the calcination temperature (Fig. 2a and b). Absorption threshold of the modified TiO₂ varies in the range of 520–566 nm. However the most important difference in the recorded optical spectra is the intensity of the absorbance signal in the visible range. Thus, for calcination at 400–450 °C and urea weight of 20–40 g, almost all the material was modified presenting an intense absorbance in the visible. On the contrary, outside these temperature and urea content ranges, the unmodified anatase phase remains strong and the modified visible light active phase forms a shoulder or even a tail in the optical

Table 1

BET surface area and porosity characteristics of the m-TiO₂ and ref-TiO₂ prepared at optimized conditions.

	m-TiO ₂	ref-TiO ₂
BET surface area (m ² /g)	175.2	48.6
Total pore volume (cm ³ /g)	0.494	0.11
Mean pore size (PSD) (nm)	8.0	7.1
Porosity (%)	75.6	31.7

absorption spectra (see for example spectra of m-TiO₂ with 30 g urea and 350 °C in Fig. 2a or that at 400 °C but with only 1 g urea in Fig. 2b). The optimal parameters for the synthesis of the modified TiO₂ with the highest response in the visible range were thus determined to be 30 g urea/15 ml tetrabutylorthotitanate and 400 °C calcination temperature, providing a threshold value for absorption in the visible range of 2.19 eV (566 nm). This narrow temperature range for the successful combustion synthesis of the VLA m-TiO₂, also frequently employed in the literature [18,19], can be understood by the thermogravimetric analysis (TGA) data (see Fig. S1). The intensive weight loss for temperatures below 350 °C suggests that the urea combustion reaction is not fully completed, while above 450 °C, organic compounds formed on the titania surface are removed. Regarding the urea content and taking into account the literature data [18,19], our results show that the fuel to oxidizer ratio φ should largely exceed the stoichiometric one (1.67), in order to optimize the materials physicochemical properties. Optimum ratio was found at $\varphi=11.4$, which stands on the flameless combustion range where the reaction is partly supported by the ambient air and is limited by oxygen diffusion, in agreement with [19]. Accordingly, the resulted vivid yellow m-TiO₂ powder synthesized under optimum temperature and urea content (shown in the inset photo of Fig. 2a) will be examined in detail in the following part of the manuscript, in comparison with the non-modified ref-TiO₂ material.

3.2. Porosity and surface area characterization

The structural and textural properties of the raw and optimally modified TiO₂ materials were investigated by N₂ adsorption-desorption isotherms at 77 K. Fig. 3 shows the obtained results analyzed by BET method for surface area and BJH pore size distribution. The surface area and porosity have been calculated for all materials and the results are given in Table 1. The isotherms (Fig. 3a) are of type IV, which is typical for mesoporous materials. In the case of the raw material a moderate surface area is derived, while the hysteresis loop indicates pore formation in the range of 5–10 nm (desorption branch). On the other hand, the N₂ isotherm of the modified TiO₂ reveals a significant increase in both the surface area and the pore volume as a result of well-developed mesoporosity. The obtained high porosity ensures enhanced reaction rates due to the high level of interaction of the reactants with the active sites. The BJH pore size distributions (Fig. 3b) of the two materials are quite similar, with an average pore diameter of 7–8 nm.

3.3. Vibrational (FTIR and Raman) analysis

Fig. 4 displays the FT-IR spectra of the m-TiO₂ sample before and after purification in comparison with the corresponding spectrum of the ref-TiO₂. In the unwashed urea-TiO₂ sample, apart from the peaks at 3400 cm⁻¹ (surface hydroxyl groups or chemisorbed water) and 1640 cm⁻¹ (bending of molecular water), a set of weak IR bands are observed in the 1200–1600 cm⁻¹ region (circled in the figure) due to C–N and C–O species along with an intense band at 2050 cm⁻¹ with fine structure, indicative of carbonaceous species in different chemical environments. The C–N and C–O bands can

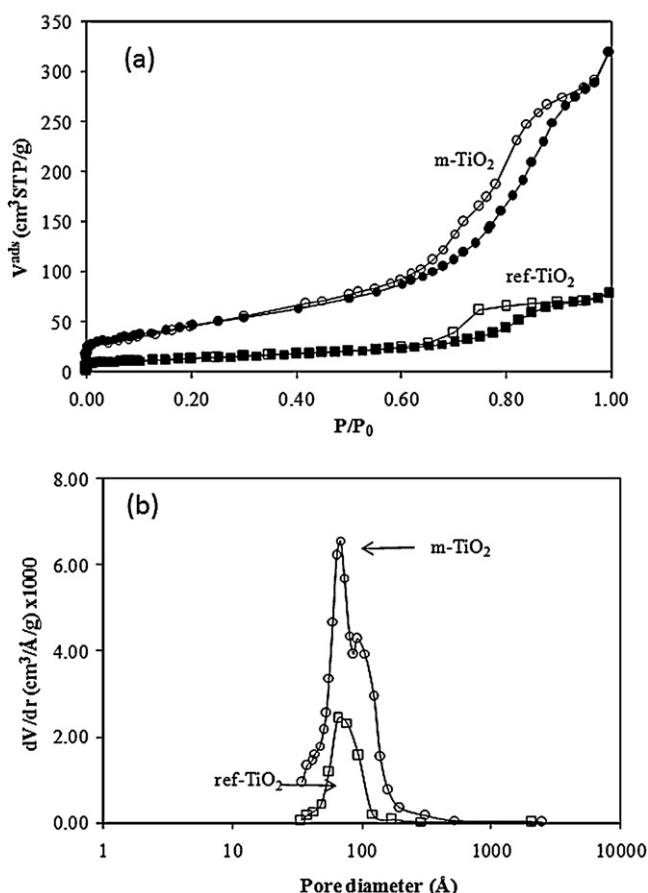


Fig. 3. (a) N_2 adsorption–desorption isotherms and (b) pore size analysis of the ref- and m-TiO₂ materials.

be attributed to urea residues remaining after the combustion reaction, as they are clearly observed in their spectra of the solution residues obtained after material purification by two centrifugation cycles (not shown), whereas only a weak feature at 1440 cm⁻¹ due to C=C bond vibrations is hardly detectable at this frequency range.

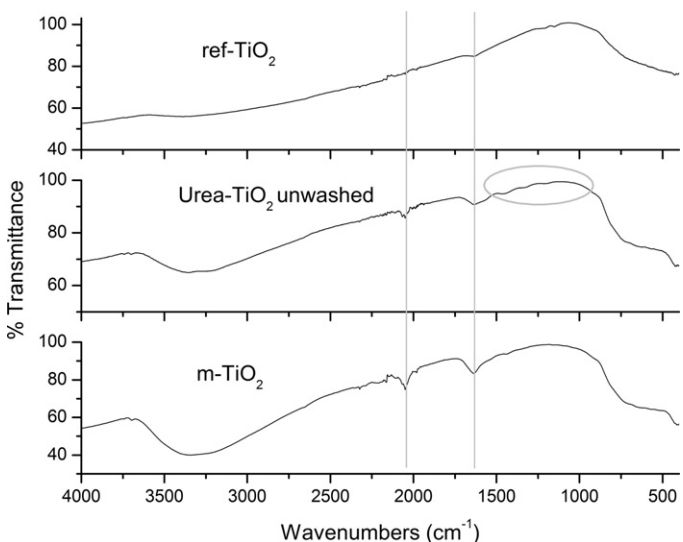


Fig. 4. FT-IR spectra of the m-TiO₂ before and after purification in comparison with the ref-TiO₂ sample. Vertical lines mark the 1640 cm⁻¹ bending of molecular water and the vibrations of the persistent organic species at 2050 cm⁻¹. Weak absorbance modes of the prewashed urea-TiO₂ are circled.

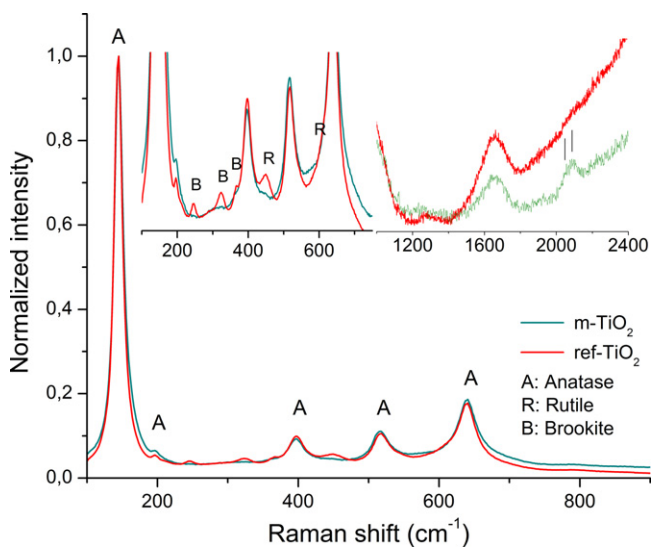


Fig. 5. Raman spectra of the modified TiO₂ compared to the reference sample at 514.5 nm. Inset graphs focus on the low frequency weak Raman peaks due to brookite and rutile minor phases of the ref-TiO₂ and on the high frequency m-TiO₂ Raman bands of interest, at 2050 and 2090 cm⁻¹.

Regarding the peak around 2050 cm⁻¹, which remains essentially unaffected by the consecutive washings, it can be rather related to the presence of C=N, C=C and C=O conjugated bonds of persistent organic species that coordinate with TiO₂ via oxygen surface atoms. Furthermore, the latter mode disappears for calcination temperatures above 450 °C (not shown), where the materials' optical absorption is suppressed in the visible range (Fig. 2a), implying a close correlation of the underlying organic species with the VLA response of the modified materials. We should mention that a vibration mode at this frequency can be also traced as a weak feature in the IR spectra of polyheptazine-TiO₂ hybrids [23], though not the spectrum of the polyheptazine unit itself, verifying that it primarily involves coordination of organics with TiO₂. Apart from the latter mode, no trace of the rich vibrational spectrum of polymeric carbon nitrides [12] (melon, melem), forming in situ at the surface of preformed titania particles from urea pyrolysis products could be identified in the present IR spectra, indicating the absence of polyheptazine species. An alternative assignment of the 2050 cm⁻¹ mode concerns NO vibration [24] from stable NO species encapsulated in microporous TiO₂ prepared by sol-gel [25], whose presence, however, is not corroborated by the EPR results (see below). On the other hand, no vibration from organics was identified in the IR spectra of the ref-TiO₂ material (the weak peak at 1152 cm⁻¹ can be attributed to O–H vibrations in Ti–O–O–H species [26]).

Raman spectra recorded for the optimal m-TiO₂ samples, shown in Fig. 5, identified the formation of single anatase nanocrystalline phase. Size of the nanocrystals was estimated to ~7 nm by projecting the values of the frequency (146.2 cm⁻¹) and FWHM (15.5 cm⁻¹) of the strongest low frequency E_g peak in standard correlation curves [27,28]. This peak presents blue shift and line broadening relative to that observed in anatase nanocrystals of large size (>20 nm) due to the breakdown of the $k=0$ Raman selection rule induced by phonon confinement [27]. In contrast, the reference sample comprises traces of the rutile/brookite polymorphic phases (Fig. 5) and anatase nanoparticles with size slightly larger than that of m-TiO₂, to about 8.5 nm. This corroborates the stabilization effect for the anatase phase and the inhibition of the anatase–brookite–rutile phase transformation by urea treatment. Furthermore, long acquisition spectra in the high frequency region 1000–2500 cm⁻¹ revealed a doublet at 2050 and 2090 cm⁻¹

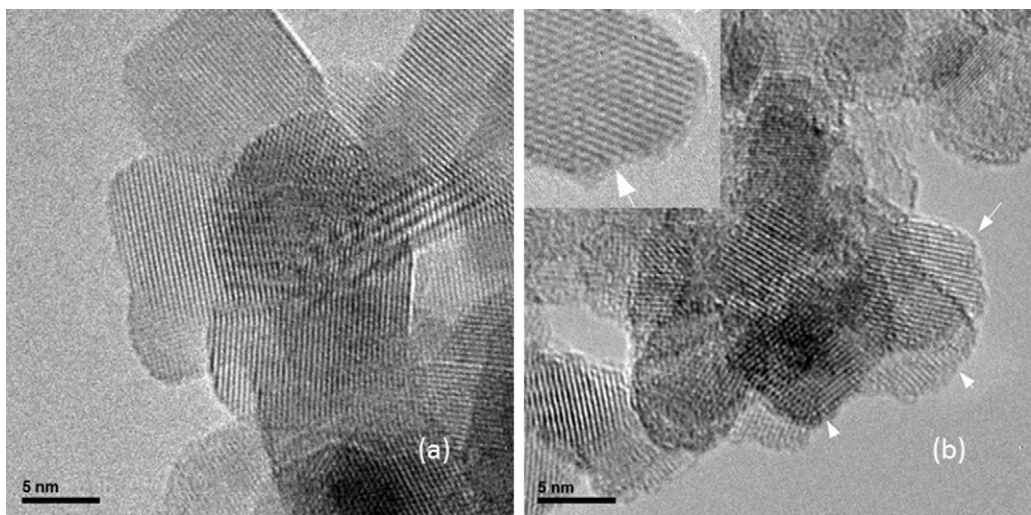


Fig. 6. TEM images of ref-TiO₂ (a) and m-TiO₂ nanoparticles (b). In (b) an amorphous shell marked by arrows covers the crystalline titania particles.

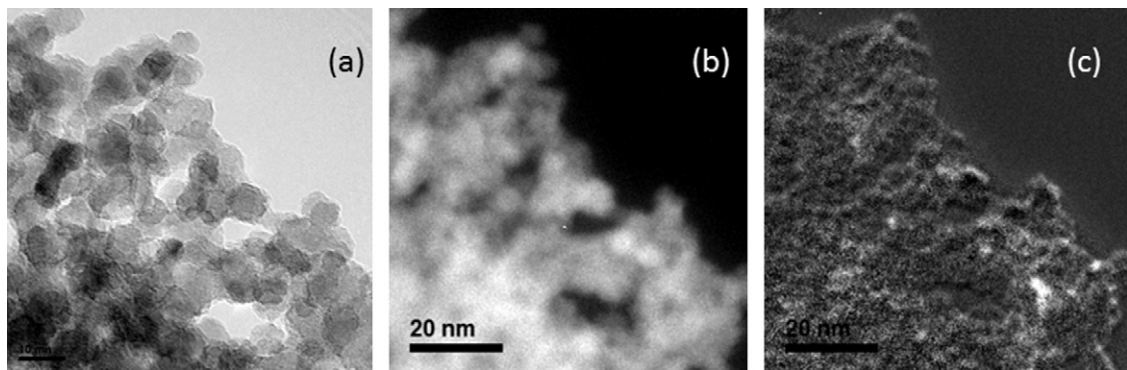


Fig. 7. TEM bright field image (a), of m-TiO₂ nanoparticles with corresponding Ti (b) and C (c) mapping analysis.

only for the m-TiO₂. The detection of weak vibrations in the 2050–2100 cm⁻¹ range, both in the resonance Raman and IR spectra verifies the presence of relatively simple structures of organic monolayers bounded on the TiO₂ surface. For both the m- and ref-TiO₂ the water bending mode at 1655 cm⁻¹ is also observed.

3.4. Microscopic TEM and SEM analysis

Following thorough cleaning, the ref- and m-TiO₂ samples were characterized by TEM. Characteristic HRTEM images are shown in Fig. 6, where particle size of about 7 nm for m-TiO₂ and 9 nm for the ref-TiO₂ are estimated, in very good agreement with the results from the Raman analysis. For m-TiO₂, an amorphous shell could be resolved (indicated by arrows in the HRTEM images and clearly shown in the inset magnified area), covering the crystalline core of the TiO₂ nanoparticles. The thickness of this shell is approximately 1 nm or even smaller. This core–shell structure is not observed in the ref-TiO₂, where the crystalline titania structure extends up to the particle surface.

EFTEM was applied for performing a spatially resolved microanalysis in the area shown in the bright field image of m-TiO₂ in Fig. 7a. The corresponding C and Ti maps from the same area are shown in Fig. 7b and c, respectively. The C map shows brighter contrast, indicating a higher C concentration, at the surface of the particles, though it is not clear whether C is also inserted inside the particle core. Moreover, EELS analysis, shown in Fig. 8, confirmed the presence of C species on the titania nanoparticles, while no

signal of N could be resolved. This can be attributed either to the low concentration of N (below the detection limit of EELS) or to N knock out by the electron beam.

Particle morphology of TiO₂ materials has been further studied by FE-SEM. It is evident in Fig. 9(a) and (b) that the ref-TiO₂ sample consists of nanoparticles (in the range of 10–20 nm) forming larger

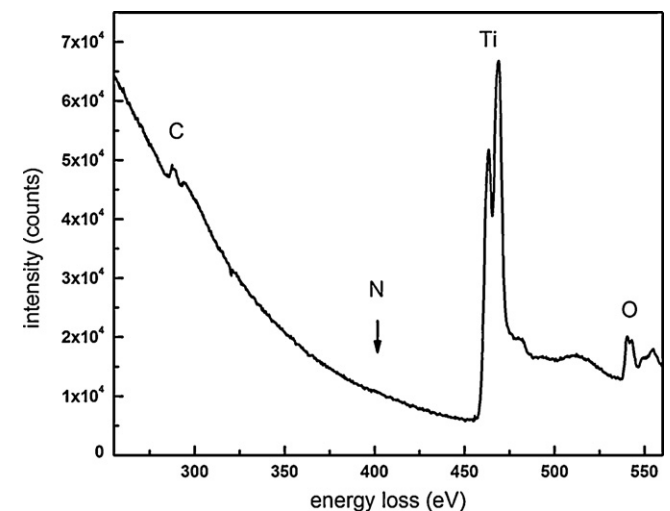


Fig. 8. EELS spectrum of the m-TiO₂ sample.

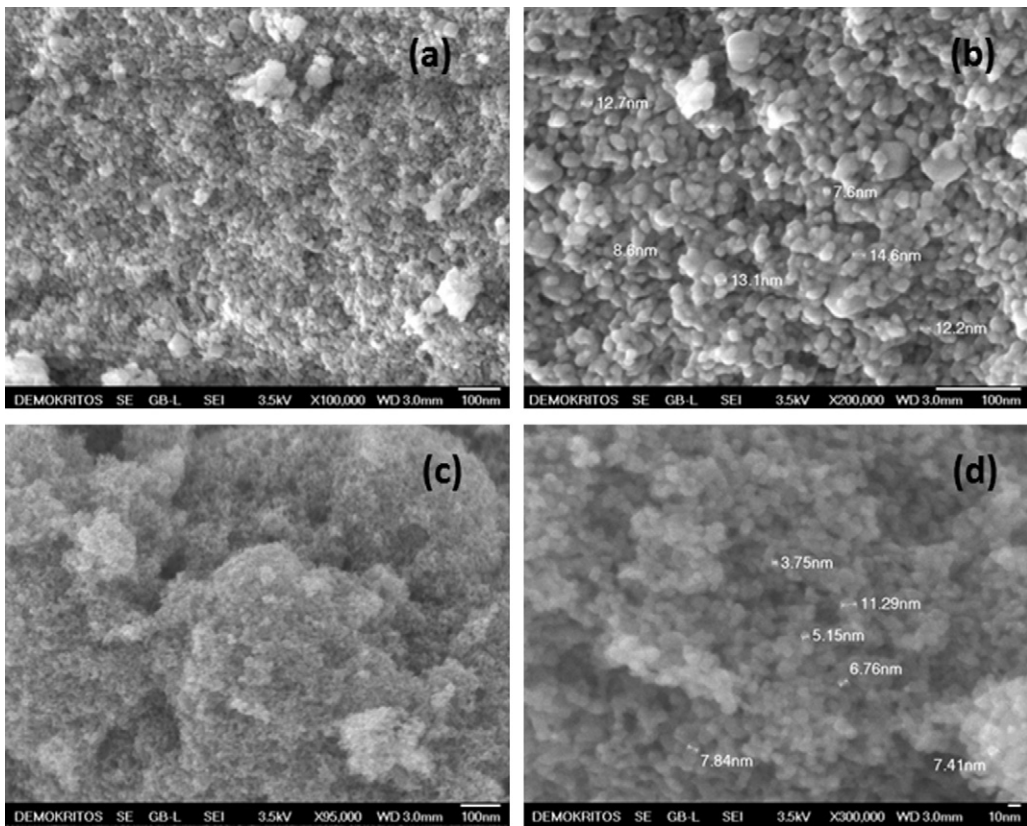


Fig. 9. HRSEM spectra of ref-TiO₂ (a and b) and m-TiO₂ (c and d) at different magnification regimes.

aggregates, with limited free volume. The presence of edged shaped particles reveals also the crystalline phase of the material. On the contrary, the m-TiO₂ particles are considerably smaller (3–10 nm) with more rounded edges, providing significant ample framework void mesopore space, as shown in Fig. 9(c) and (d). This result is consistent with the textural mesoporosity determined by the N₂ porosimetry analysis. Furthermore, the absence of charging effects in the latter case may be attributed to the inorganic core–organic shell structure which has been identified by HRTEM.

3.5. XPS analysis

Wide XPS scans (0–1400 eV) for the two samples are presented below in Fig. 10. Features related to Ti, O, C, N are labeled. The inset graphs in Fig. 10 show detailed spectra of the C1s and N1s peaks. The main C1s peak was originally found at a BE of ~285.9 eV. However, due to possible charging effects a correction of 1.4 eV was overall applied to the spectra of both samples. This is a common practice, in order to fix the adventitious C peak to a BE of ~284.5 eV. The second peak at around 288 eV, which after the fitting analysis was observed at slightly more positive energy for m-TiO₂ relative to ref-TiO₂, suggests that carbon is bound to oxygen and/or nitrogen species [29], in consistency with presence of carbonate species [20,30]. No peak around 281–282 eV due to Ti–C bonding was observed excluding the possibility of substitutional C doping for oxygen atoms in the anatase lattice [31].

The N1s region for both samples exhibits a peak located at ~400 eV. The intensity of the N peak in the ref-TiO₂ sample is larger than in the modified m-TiO₂ sample, due to the nitrogen originating from nitrates, either chemisorbed [32] or forming oxynitrides [33]. However, during the combustion of urea in the m-TiO₂ sample certain amount of N has escaped as N₂ gas and the total N concentration is limited to the organic species formed on the surface of

TiO₂ giving rise to C–N bonds [28] with sp² or sp³ hybridization. The shift toward higher BE of the N–O, N–C and Ti–N–O (~400 eV) configuration as compared to Ti–N–Ti (~396) is due to the more electronegative nature of O and C as compared to Ti. The presence of a major nitride compound is excluded since there is not a clearly resolved feature present at BE ~396.3, where Ti–N bonds should appear. Moreover, NO adsorption and/or interstitial nitrogen which also give N1s XPS signal at about 400 eV [3,6] are also precluded for both samples based on the EPR results (vide infra). Finally, the Ti2p region (see Fig. S3) exhibits a doublet peak due to spin-orbit

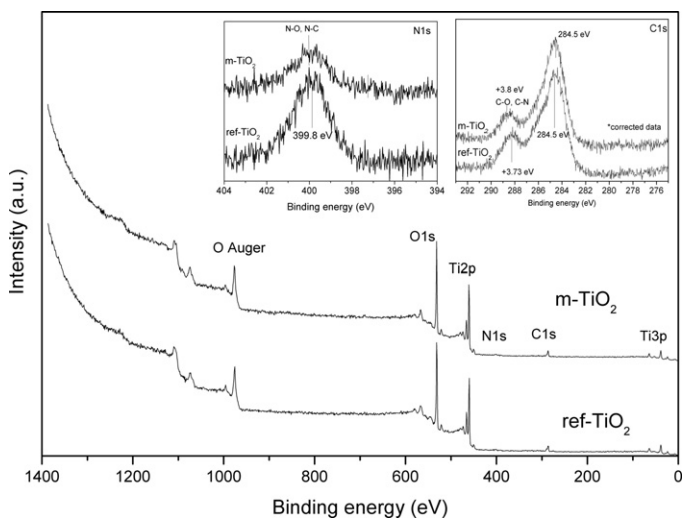


Fig. 10. Wide XPS spectra of m-TiO₂ and ref-TiO₂ samples. Detailed spectra in the C1s and N1s energy regions are shown in the inset graphs.

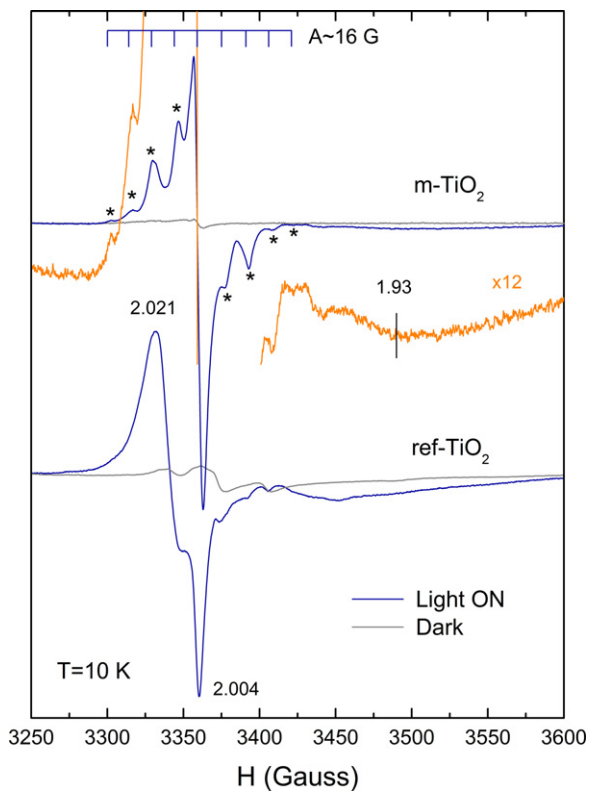


Fig. 11. EPR spectra of the optimal modified TiO₂ in comparison with the reference sample under dark conditions and after visible light illumination, at 10 K.

splitting with common binding energies for the two samples. The BE position of the 2p_{3/2} peak at ~458.4 eV, agrees well with the presence of Ti⁴⁺ ions in TiO₂. Based on the XPS analysis, we may conclude that while the amounts of C and N species is comparable for both m-TiO₂ and ref-TiO₂, the subtle differences of the N1s and C1s spectra between the two samples essentially arise from their incorporation into the m-TiO₂ shell, while leaving intact the TiO₂ core as identified by the performed HRTEM analysis.

3.6. EPR spectroscopic characterization

The formation of localized paramagnetic centers in the ref- and m-TiO₂ samples was investigated by EPR spectroscopy under visible light illumination provided by a LED source at 440–460 nm. Fig. 11 shows the EPR spectra of the optimal m-TiO₂ in comparison with those of the reference sample under dark and visible light illumination conditions, at 10 K.

Visible light illumination of the modified TiO₂ resulted in a marked enhancement (ca. 20-fold increase) of the EPR signal leading to an extended resonance spectrum centered at $g = 2.005$. Most importantly, the visible light induced EPR spectrum comprised a set of eight regularly spaced resonance lines around the central EPR line, indicative of an extended hyperfine structure with a splitting constant $A \sim 16$ G. This type of EPR spectrum is entirely different from that of the ref-TiO₂ sample, where visible light illumination resulted in the appearance of intense anisotropic EPR spectra at $g > 2.0$ arising from the photo-induced formation of surface trapped hole centers (O^-) and superoxide anions (O_2^-) in the presence of oxygen, similar to conventional sol-gel TiO₂ [5,31]. This further corroborates that N and C species have distinctly different origins in ref-TiO₂ and m-TiO₂, despite their quantification at similar amounts by XPS. Most importantly, the observed EPR spectrum in m-TiO₂ differs from the characteristic ¹⁴N hyperfine triplet EPR spectrum arising from single nitrogen species in N-doped TiO₂

prepared by other synthetic routes and nitrogen precursors [6], suggesting a different mechanism for the visible light activation of m-TiO₂ from N2p intraband gap states created of the TiO₂ lattice. Furthermore, the observed EPR spectrum is essentially different from that of paramagnetic NO molecules frequently adsorbed in N-doped TiO₂ [24]. Specifically, the EPR spectrum of NO radicals is characterized by a rhombic g-tensor with $g_{xx} \approx g_{yy} \approx 2.00$ and ¹⁴N ($I = 1$) hyperfine constants $A_x < 1$ G and $A_y \sim 32$ G that may account for only one pair of the observed EPR lines, while its $g_{zz} \approx 1.93$ component was not observed in the present case. Moreover, the EPR signal of trapped NO species in nitrogen doped TiO₂ has been reported to disappear at temperatures higher than 170 K [24] and not to be affected by visible light excitation [34], whereas the present EPR signal is clearly observable up to room temperature, implying rather long spin-lattice relaxation times, and emerges only upon visible light excitation.

Although the exact origin of the observed EPR spectrum that may comprise more than one paramagnetic species cannot be readily traced, its visible light activation together with the presence of hyperfine structure due to the most abundant ¹⁴N ($I = 1$) and or ¹H ($I = 1/2$) nuclei indicates that it originates from the light induced excitation of organic (C, N, H) radicals (the 1:2:3:2:1 EPR pattern of s-triazine radicals may not solely account for the observed EPR spectrum [35,36]) that reside on the titania surface and act as photosensitizers of TiO₂ under visible light. In addition, a very broad EPR signal was observed at $g = 1.93\text{--}1.95$ for both the urea modified and reference TiO₂ (Fig. 11). This EPR signal is characteristic of trapped electrons in localized anatase Ti³⁺ surface states [37]. The wide distribution of the underlying energy levels below the anatase conduction band, renders them populated by the sub-band gap illumination (~2.75 eV) provided by the LED source, even for the ref-TiO₂ material. The contribution of these anatase Ti³⁺ surface states is therefore not expected to be very effective in the visible light photocatalytic activity of the urea modified TiO₂.

3.7. Photocatalytic degradation and demethylation of MB

Evaluation of the materials photocatalytic performance was examined for the degradation of methylene blue under UVA, daylight and visible light irradiation for 120 min. Fig. 12 shows the progression of the MB photocatalytic degradation, including dye adsorption by the ref- and the m-TiO₂ and the Evonik P25 photocatalytic powder for the three different illumination sources and Figure S4 shows the absorption spectra of the solution at different stages of the photocatalytic experiment. The obtained results showed that the ref-TiO₂ material has very weak photocatalytic response under visible light illumination and is less active than the m-TiO₂ under daylight illumination, reflecting its marginal response in the visible spectral range. On the other side, it performs quite well under UV irradiation where, after 2 h, the photocatalytic degradation has reached the levels attained by Evonik P25. The behavior of P25 is quite similar with good photocatalytic response only under UVA and daylight. On the opposite, the modified TiO₂ exhibited significant photocatalytic activity under pure visible light. Hence, modification of the TiO₂ surface employing urea during the sol-gel synthesis under optimal loading and thermal treatment conditions is concluded as an efficient means to improve the light harvesting ability and photocatalytic activity of titania in the visible range.

Methylene blue is a cationic dye pollutant resistant to natural degradation. According to the literature [38,39], the UV photocatalysis procedure degrades MB to smaller organic substances until total mineralization to H₂O, CO₂, and other inorganic species. During photocatalysis hypsochromic effects take place implemented in blue shifts of spectral bands, resulting from N-demethylation of the dimethylamino group in MB. This effect occurs concomitantly

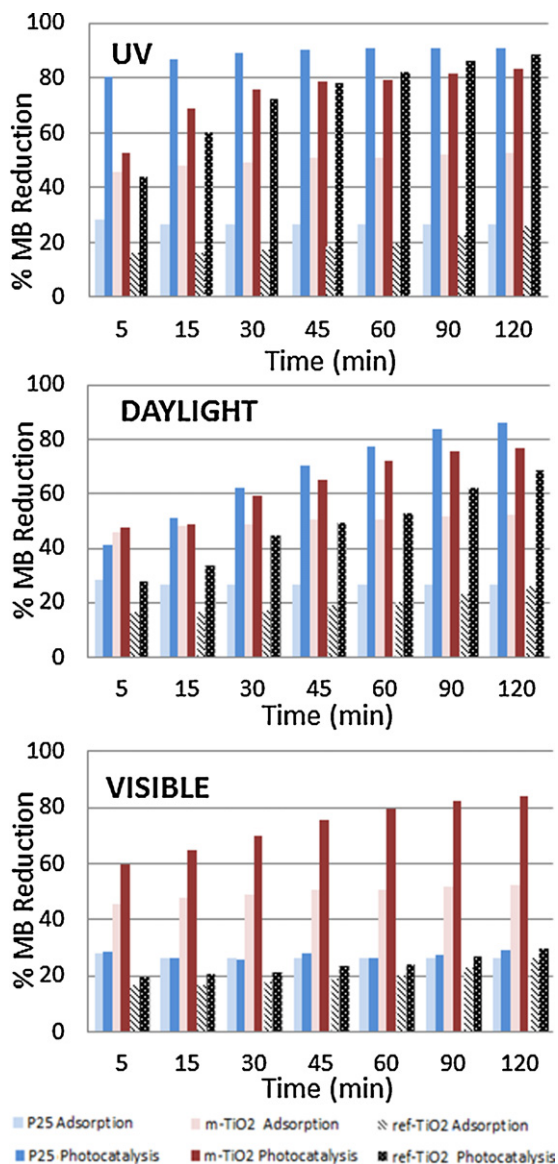


Fig. 12. Methylene blue reduction in the solution due to adsorption and photocatalysis by P25, the optimal m-TiO₂ and ref-TiO₂, under UVA (350–390 nm), daylight (350–750 nm) and visible (440–460 nm) light illumination.

with the oxidative photocatalytic degradation of the phenothiazine chromophore ring structure of MB which is attested by the decrease of the absorption peak at 292 nm with irradiation time, most prominently observed during the initial irradiation period. As described in previous studies [38,39], the N-demethylation of MB occurs by the formation of intermediate species with shifted absorption band peaks according to the following pathway: (i) Azure B (648–654 nm), (ii) Azure A (620–634 nm), (iii) Azure C (608–612 nm), and (iv) Thionine (602.5 nm). As seen in Fig. 13 for the m-TiO₂, the degradation of MB was done in a stepwise manner and the spectral band at 664 nm blue-shifts after 120 min by as much as 42 nm for LED illumination (from 664 to 622 nm), and 48.5 nm (from 664 to 615.5 nm) for daylight illumination and 62 nm for UV irradiation (from 664 to 602 nm). Accordingly, we conclude that, by completing the 2 h photocatalytic experiments, apart from the degradation of the phenothiazine chromophore ring, partial (under LED and daylight irradiation) or full (under UV irradiation) demethylation of MB occurs. Intermediates of Azure A and/or Azure C are formed in the first case and thionine in the last.

Due to the excellent photocatalytic performance of Evonic P25 photocatalytic powder under UV it was hard to define a clear peak in the absorbance spectrum in order to measure the blue-shift of the 664 nm characteristic peak of MB. However daylight irradiation resulted in 52 nm shift, corresponding to Azure C as the main degradation product (it was not possible to detect absorption of thionine under the prevailing conditions most probably due its tendency to get adsorbed onto the TiO₂ surface) while visible light illumination with the LED sources did not affect the wavelength of the MB absorption peak, as expected. Similarly for ref-TiO₂, visible light illumination did not shift the MB peak, while daylight and UV irradiation resulted in 29 and 52 nm shifts, respectively.

The photocatalytic results were compared to literature data obtained when crystalline TiO₂ and thiourea are mixed and calcined at 400 °C (namely PreCal TiO₂-TU). Such a comparison shows that for a total 2 h experiment under visible light irradiation, a 13 nm blue shift of the MB absorption peak is observed in comparison to the 42 nm for the m-TiO₂ sample synthesized in this study under similar conditions. This fact concurs with the better photocatalytic efficiency of the m-TiO₂ photocatalyst, 84%, relative to PreCalTiO₂-TU, 65%. The m-TiO₂ material developed in this work also outperforms carbon modified TiO₂ photocatalysts prepared by post treatment of crystalline TiO₂ [40]. This very efficient performance is attributed to the effective decoration of TiO₂ particles with simultaneously grown carbonaceous species acting as sensitizers. Similar structures achieved by combustion synthesis have produced some of the best MB photocatalytic results under full sunlight irradiation [18,41] while in the current research in this area, judicious morphologies, like crystalline TiO₂ core with graphene shell, are developed as the next generation VLA photocatalysts [29].

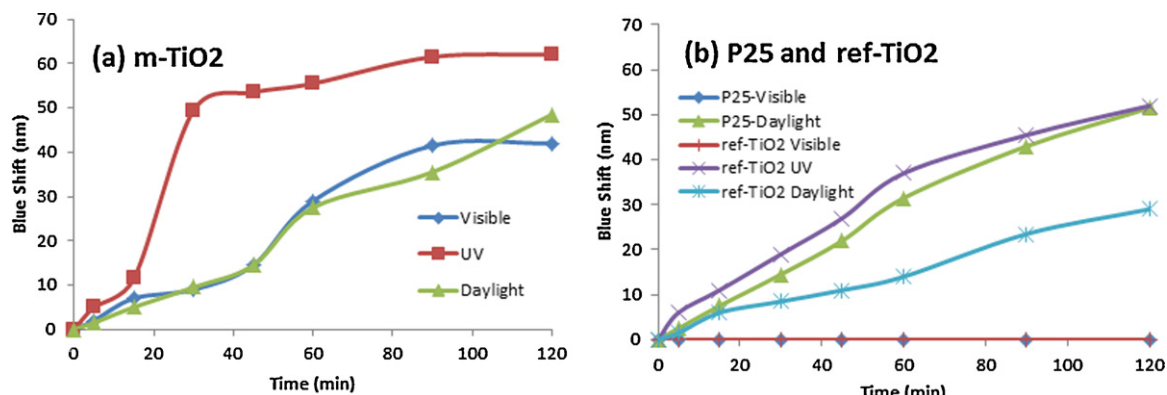


Fig. 13. Shift of MB absorption peak due to demethylation for m-TiO₂ (a) as well as ref-TiO₂ and P25 (b).

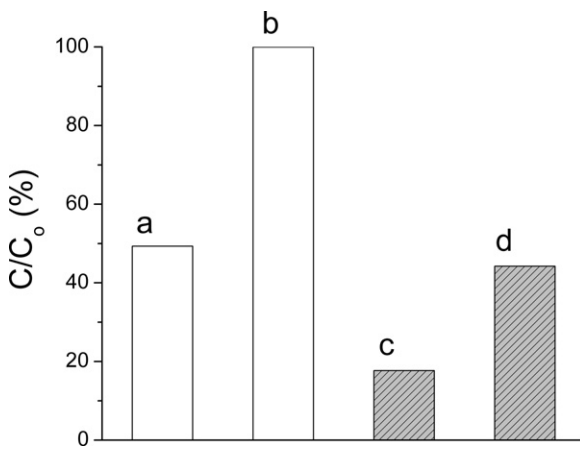


Fig. 14. Relative concentration (%) of MB solution: after adsorption (a)—desorption (b) from m-TiO₂ in dark; after adsorption/photocatalysis on m-TiO₂ under visible light illumination (c), followed by desorption in dark (d).

The modified titania photocatalyst was tested for possible deactivation effects by performing three subsequent photocatalytic experiments under visible light illumination, lasting 1 h each. In between the photocatalytic cycles, two centrifugation steps were carried out in order to separate the photocatalyst from the solution before and after desorption of the pollutant, thereafter, care was taken to keep the photocatalyst to MB solution ratio constant. A perfect reproducibility of the photocatalytic efficiency (within 2% error range) was evidenced; rendering the materials excellent candidates for long lasting photocatalytic treatment of polluted water. Moreover, in order to confirm the photocatalytic activity of the modified TiO₂ photocatalyst under visible light irradiation, the final overall concentration of the MB pollutant (MB inside the solution and adsorbed on the photocatalysts) was tested after desorption of MB from the m-TiO₂ surface. The experiment was conducted according to the method described in [5], and the results are presented in the histogram graph of Fig. 14. In detail, a suspension of m-TiO₂ photocatalyst (1 g/L) in oxygenated MB (2 mg/L) aqueous solution was prepared. The solution was left for 1 h under vigorous stirring and in dark so that the pollutant got well adsorbed on TiO₂. Then the relative concentration of the MB (C/C_0) was measured photometrically at 49.3% (point a of Fig. 14). In turn the solution's pH was adjusted to 2.8 using the appropriate quantity of 1 N HCl followed by 1 h of stirring under dark, in order to fully desorb MB from m-TiO₂ as shown by the nearly 100% recovery of the MB concentration (point b of Fig. 14). This procedure was repeated but with constant illumination of the solution with visible light during the MB adsorption step (points c in Fig. 14). With the completion of 1 h, MB concentration reached a 17.6% percentage of the initial concentration. However, after the addition of the HCl and vigorous stirring in dark, the MB concentration recovered at only 44.2% of the initial value (point d of Fig. 14), indicating a strong net photocatalytic degradation of MB by visible light illumination. The above enhanced photocatalytic performance of the synthesized material is an inherent property and not specific to MB molecule. In fact, preliminary experiments also confirmed that the m-TiO₂ photocatalyst shows high efficiency for the degradation of a series of model water pollutants with varied chemical structure and functionalities including methyl orange (MO), diphenhydramine (DP) pharmaceutical and microcystine-LR (MC-LR) under visible light illumination.

4. Conclusion

Nanostructured modified TiO₂ was synthesized by gel combustion of a nitrated alkoxide solution mixed with urea fuel. The

modified materials were optimized in terms of solar light harvesting by controlling the urea content and the calcination temperature, thus reaching an absorption threshold of 2.19 eV and very high absorbance values. The visible light activation of the material is attributed to the formation of monolayers of carbonaceous species which cover TiO₂ core anatase nanoparticles. This organic shell is clearly observed in HRTEM images as a uniform defected structure and supported by XPS, EELS and elemental EFTEM mapping as well by the Raman and NIR vibrations in the 2050–2100 cm⁻¹ range which are rather related to the presence of C=N, C=C and C=O conjugated bonds. The small size of the m-TiO₂ particles and the porous character of the organic layer provide ample void mesopore space with very high values of BET surface area (175.2 m²/g) and porosity (75.6%). EPR measurements recorded a signal with extended hyperfine structure attributed to the most abundant ¹⁴N ($I=1$) and/or ¹H ($I=1/2$) nuclei originating from organic (C, N, H) radicals. This signal presents a 20-fold increase upon visible light illumination indicating light induced excitation of the organic radicals. For comparison, ref-TiO₂ materials were synthesized without the addition of urea and presented none of the outstanding physicochemical properties described above for m-TiO₂. Since the amount of C and N estimated by elemental analysis and XPS was quite similar for both samples (modified and unmodified), we conclude that the salient feature of m-TiO₂ is its distinct core-shell structure.

The modified hybrid material presents significant photocatalytic degradation of methylene blue dye, especially under visible light, where it far outperforms over the benchmark Degussa P25 and excellent photocatalytic reproducibility. This behavior of the modified material is attributed to the modification of the photocatalyst surface by the organic sensitizer as well as to the retardation of recombination effects due to the small nanoparticle size and the improved charge separation at the inorganic/organic heterojunction. Among the advantages of the method are the controlled, uniform and fully repeated morphology and its easy adaption in VLA photocatalytic technologies such as modified photocatalytic membranes for water purification.

Acknowledgements

This work was funded by the European Commission (Clean Water – grant agreement number 227017). Clean Water is a collaborative project co-funded by the Research DG of the European Commission within the joint RTD activities of the Environment and NMP Thematic Priorities.

Appendix A. Supplementary data

Supplementary data associated with this article can be found, in the online version, at <http://dx.doi.org/10.1016/j.apcatb.2012.10.007>.

References

- [1] A. Fujishima, K. Honda, Nature 238 (1972) 37–38.
- [2] A. Fujishima, X. Zhang, D.A. Tryk, Surface Science Reports 63 (2008) 515–582.
- [3] M. Pelaez, N.T. Nolan, S.C. Pillai, M.K. Seery, P. Falaras, A.G. Kontos, P.S.M. Dunlop, J.W.J. Hamilton, J.A. Byrne, K. O'Shea, M.H. Entezari, D.D. Dionysiou, Applied Catalysis B: Environmental 125 (2012) 331–349.
- [4] M. Pelaez, P. Falaras, V. Likodimos, A.G. Kontos, A.A. de la Cruz, K. O'Shea, D.D. Dionysiou, Applied Catalysis B: Environmental 99 (2010) 378–387.
- [5] C. Han, M. Pelaez, V. Likodimos, A.G. Kontos, P. Falaras, K. O'Shea, D.D. Dionysiou, Applied Catalysis B: Environmental 107 (2011) 77–87.
- [6] C. Di Valentin, E. Finazzi, G. Pachioni, A. Selloni, S. Livraghi, M.C. Paganini, E. Giannello, Chemical Physics 339 (2007) 44–56.
- [7] X. Chen, L. Liu, P.Y. Yu, S.S. Mao, Science 331 (2011) 746–750.
- [8] S.G. Kumar, L.G. Devi, Journal of Physical Chemistry A 115 (2011) 13211–13241.
- [9] R. Leary, A. Westwood, Carbon 49 (2011) 741–772.
- [10] V.N. Kuznetsov, N.J. Serpone, Journal of Physical Chemistry C 113 (2009) 15110–15123.

- [11] D. Mitoraj, H. Kisch, *Angewandte Chemie* 47 (2008) 9975–9978.
- [12] D. Mitoraj, H. Kisch, *Chemistry: A European Journal* 16 (2010) 261–269.
- [13] A.I. Kontos, A.G. Kontos, Y.S. Raptis, P. Falaras, *Physica Status Solidi (RRL)* 2 (2008) 83–85.
- [14] R. Vine, G. Madras, *Journal of Indian Institute of Science* 90 (2010) 189–230.
- [15] K. Nazarene, G. Sivalingam, M.S. Hegde, G. Madras, *Applied Catalysis B: Environmental* 48 (2004) 83–93.
- [16] K. Nagaveni, M.S. Hegde, N. Ravishankar, G.N. Subbanna, G. Madras, *Langmuir* 20 (2004) 2900–2907.
- [17] P.R. Potti, V.C. Srivastava, *Industrial and Engineering Chemistry* 51 (2012) 7948–7956.
- [18] S.-L. Chung, C.-M. Wang, *Journal of Sol-Gel Science and Technology* 57 (2011) 76–85.
- [19] K. Sivarajanji, C.S. Gopinath, *Journal of Materials Chemistry* 21 (2011) 2639–2647.
- [20] T. Ohno, T. Tsubota, K. Nishijima, Z. Miyamoto, *Chemistry Letters* 33 (2004) 750–751.
- [21] J.S. Lee, K.H. You, C.B. Park, *Advanced Materials* 24 (2012) 1084–1088.
- [22] P. Zabek, J. Eberl, H. Kisch, *Photochemical and Photobiological Sciences* 8 (2009) 264–269.
- [23] M. Bledowski, L. Wang, A. Ramakrishnan, O.V. Khavryuchenko, V.D. Khavryuchenko, P.C. Ricci, J. Strunk, T. Cremer, C. Kolbeck, R. Beranek, *Physical Chemistry Chemical Physics* 13 (2011) 21511–21519.
- [24] T.P. Ang, C.S. Toh, Y.-F. Han, *Journal of Physical Chemistry C* 113 (2009) 10560–10567.
- [25] S. Livraghi, M.R. Chierotti, E. Giannello, G. Magnacca, M.C. Paganini, G. Cappelletti, C.L. Bianchi, *Journal of Physical Chemistry C* 112 (2008) 17244–21725.
- [26] G. Mattioli, F. Filippone, A.A. Bonapasta, *Journal of the American Chemical Society* 128 (2006) 13772–13780.
- [27] A.I. Kontos, A.G. Kontos, D.S. Tsoukleris, G.D. Vlachos, P. Falaras, *Thin Solid Films* 515 (2007) 7370–7375.
- [28] V. Likodimos, T. Stergiopoulos, P. Falaras, J. Kunze, P. Schmuki, *Journal of Physical Chemistry C* 112 (2008) 12687–12696.
- [29] X. Li, J. Zhang, L. Shen, Y. Ma, W. Lei, Q. Cui, G. Zou, *Applied Physics A* 94 (2009) 387–392.
- [30] D. Zhao, G. Sheng, C. Chen, X. Wang, *Applied Catalysis B: Environmental* 111–112 (2012) 303–308.
- [31] G. Liu, C. Han, M. Pelaez, D. Zhu, S. Liao, V. Likodimos, N. Ioannidis, A.G. Kontos, P. Falaras, P.S.M. Dunlop, J.A. Byrne, D.D. Dionysiou, *Nanotechnology* 23 (2012) 294003.
- [32] G. Abadias, F. Paumier, D. Eyidi, P. Guerin, T. Girardeau, *Surface and Interface Analysis* 42 (2010) 970–973.
- [33] P. Romero-Gomez, V. Rico, A. Borrás, A. Barranco, J.P. Espinós, J. Cotrino, A.R. González-Elipe, *Journal of Physical Chemistry C* 113 (2009) 13341–13351.
- [34] S. Livraghi, M.C. Paganini, E. Giannello, A. Selloni, C. Di Valentini, G. Pacchioni, *Journal of the American Chemical Society* 128 (2006) 15666–15671.
- [35] A. O'Connell, I.D. Podmore, M.C.R. Symons, J.L. Wyatt, F. Neugebauer, *Journal of the American Chemical Society, Perkin Transactions 2* (1992) 1403–1407.
- [36] C.J. Rhodes, H.A. Moynihan, *Magnetic Resonance in Chemistry* 39 (2001) 133–136.
- [37] D.C. Hurum, K.A. Gray, T. Rajh, M.C. Thurnauer, *Journal of Physical Chemistry B* 109 (2005) 977–980.
- [38] T. Zhang, T. Oyama, A. Aoshima, H. Hidaka, J. Zhao, N.J. Serpone, *Journal of Photochemistry and Photobiology A: Chemistry* 140 (2001) 163–172.
- [39] T.P. Ang, Y.M.J. Chan, *Journal of Physical Chemistry C* 115 (2011) 15965–15972.
- [40] E. Kusiak-Nejman, M. Janus, B. Grzmil, A.W. Morawski, *Journal of Photochemistry and Photobiology A: Chemistry* 226 (2011) 68–72.
- [41] Q. Xiao, J. Zhang, C. Xiao, Z. Si, X. Tan, *Solar Energy* 82 (2008) 706–713.